Optical Properties of Two Complementary Samples of Intermediate Seyfert Galaxies

Benedetta Dalla Barba [1,2,*] , **Marco Berton** [3] , **Luigi Foschini** [2] , **Giovanni La Mura** [4,5] , **Amelia Vietri** [6]
and Stefano Ciroi [6]

1 Dipartimento di Scienza e Alta Tecnologia (DiSAT), Università degli studi dell'Insubria, 22100 Como, Italy
2 Istituto Nazionale di Astrofisica (INAF), Osservatorio Astronomico di Brera, 23807 Merate, Italy;
   luigi.foschini@inaf.it
3 European Southern Observatory (ESO), Santiago de Chile 19001, Chile
4 Osservatorio Astronomico di Cagliari, Istituto Nazionale di Astrofisica (INAF), 09047 Selargius, Italy;
   glamura@lip.pt
5 Laboratório de Instrumentação e Física Experimental de Partículas (LIP), 1649-003 Lisboa, Portugal
6 Dipartimento di Fisica e Astronomia, Università di Padova, 35122 Padova, Italy;
   amelia.vietri@phd.unipd.it (A.V.); stefano.ciroi@unipd.it (S.C.)
* Correspondence: benedetta.dallabarba@inaf.it

Abstract: We present first results of the analysis of optical spectra of two complementary samples of Seyfert galaxies (Seyferts). The first sample was extracted from a selection of the 4th Fermi Gamma-ray Large Area Telescope (4FGL) catalog and consists of 11 γ-ray-emitting jetted Seyfert galaxies. The second one was extracted from the Swift-BAT AGN Spectroscopic Survey (BASS) and is composed of 38 hard-X-ray-selected active galactic nuclei (AGN). These two samples are complementary, with the former being expected to have smaller viewing angles, while the latter may include objects with larger viewing angles. We measured emission-line ratios to investigate whether the behavior of these Seyferts can be explained in terms of obscuration, as suggested by the Unified Model (UM) of AGN, or if there are intrinsic differences due to the presence of jets or outflows, or due to evolution. We found no indications of intrinsic differences. The UM remains the most plausible interpretation for these classes of objects, even if some results can be challenging for this model.

Keywords: Seyfert galaxies; intermediate Seyfert; AGN; optical spectroscopy

1. Introduction and Motivation

Seyfert galaxies (Seyferts) were first introduced by Carl Keenan Seyfert in 1943 [1], when he noted the presence of unusual broad emission lines in the optical spectra of a sample of nearby galaxies. Following this seminal work, other authors [2–5] have emphasized the need to categorize Seyferts into at least two groups: Seyfert 1 and Seyfert 2 (Sy1 and Sy2, respectively). Sy1s correspond to active galactic nuclei (AGN) with low inclination or nearly face-on orientations, where the broad-line region (BLR) is visible in optical spectra and produces a broad component in the permitted lines, such as Balmer lines. In contrast, Sy2s have high inclination or nearly edge-on orientations. This orientation difference is not linked to the host galaxy properties but to the presence of a dusty torus, which completely obscures the BLR in Sy2, allowing for only the narrow lines from the Narrow-Line Region (NLR) to be visible in the spectra. This interpretation of Seyferts is based on the Unified Model (UM) introduced by Robert Antonucci [6]; see also [7,8]. According to this model, the distinction between Sy1 and Sy2 galaxies is sharp, although there are numerous sources with intermediate properties observed to date. These sources have been classified as Intermediate Seyferts (ISs), defined as Seyferts with spectral properties falling between types 1 and 2 [9,10]. In the spectra of IS galaxies, Balmer lines exhibit a composite profile composed of a narrow peak from the NLR superimposed on a broad component from the

BLR. Consequently, IS galaxies can be further subdivided based on the prominence of the BLR relative to the NLR in the permitted lines. This division results in categories such as Sy1.2, Sy1.5, Sy1.8, and Sy1.9, with the sequence representing a decreasing contribution of the broad component compared with the narrow one. The determination of an IS galaxy type can be achieved using two methods, the first of which is

$$R = \frac{[\text{O III}]\lambda 5007}{\text{H}\beta_{\text{broad}}}, \tag{1}$$

where $[\text{O III}]\lambda 5007$ is the line flux of the oxygen line, the same for $\text{H}\beta_{\text{broad}}$ [11,12]. Here, we identify four classes using Table 1.

Table 1. Seyfert classification according to Mark Whittle [11]. See text for details.

Seyfert Type	Condition
Sy1	$R \leq 0.3$
Sy1.2	$0.3 < R \leq 1$
Sy1.5	$1 < R \leq 4$
Sy1.8	$R > 4$
Sy1.9	Broad component only in Hα

In the second method, we directly calculate the type with [12]

$$\text{Type} \sim 1 + \left[\frac{I(H\alpha_{\text{narrow}})}{I(H\alpha_{\text{total}})} \right]^{0.4} \tag{2}$$

using the properties of the sole Hα line. Here, I denotes the intensity of the involved lines, e.g., the narrow and the total components of Hα. The aim, in both the cases, is to have a comparison between the narrow and the broad/total components of the lines.

In the UM framework, ISs are positioned between Sy1 and Sy2 galaxies, suggesting that they represent AGN with intermediate viewing angles and partial obscuration. More recently, some authors have paid attention to the limitations and challenges of explaining Seyfert galaxy properties solely within the UM framework [13]. This study centered on J2118–0732, which is the first confirmed non-local IS residing within an interacting late-type galaxy, capable of maintaining powerful relativistic jets detectable at γ-ray energies. The probability of observing such a γ-ray source is exceedingly low within the UM framework. More commonly, relativistic jets are observable in Sy1 due to the alignment of the jet with the observer's line of sight, leading to enhanced emissions through the beaming process. However, a small fraction of AGN, about 2.8% of γ-ray-detected AGN, exhibit misaligned jets [14]. The intriguing question that arises is why these misaligned sources constitute such a minor portion of γ-ray-emitting AGN. Several potential explanations can be considered: these objects may appear as ISs, but their line profiles are modified by intrinsic processes unrelated to obscuration, or their scarcity may be due to the faintness of γ-emissions when they are not aligned with the observer's line of sight, possibly as a result of instrumental limitations.

From these observations, one can conclude that the UM alone does not provide a sufficient explanation for the differences among Seyfert classes. One possible approach is the introduction of a hybrid model that combines the extrinsic representation (the UM) with more intrinsic factors, such as the presence of relativistic jets, outflows, or evolutionary processes. Jets can significantly alter the spectral characteristics of the source, especially when dealing with changing-look AGN (CL-AGN). In the most common scenario, CL-AGN initially exhibit a spectrum dominated by emission lines, which then transforms into a featureless spectrum, and vice versa [14]. However, this transformation is not the only possibility. Variations in obscuration or accretion rates can also induce changes in the optical spectrum, particularly in the BLR of the emission lines [15,16]. Alternatively, outflows can reshape the profiles of the

lines, such as [O III]$\lambda\lambda$4959, 5007. These oxygen lines often display blue bumps or additional components, which are associated to outflows. This can have a significant impact on the classification process, given that [O III]λ5007 is one of the most critical lines for both manual and automated (machine learning) classification methods [17]. Lastly, one can consider an evolutionary scenario in which a peculiar class of Seyferts (Narrow-Line Seyfert 1, NLS1) can be seen as young or rejuvenated quasars that transition into their mature phase and follow an evolution path known as the blazar sequence [18,19].

Another aspect related to the intrinsic hypothesis is the difficulty in classifying Seyfert types accurately. We used the most common classification methods, as defined in Equations (1) and (2), both of which rely on distinguishing between the emission from the BLR and the NLR. However, a significant problem arises when the spectrum has a low Signal-to-Noise ratio (S/N), as the edges of each emission component can overlap, potentially leading to misclassification. This highlights the limitations of the current classification methods and underscores the need for further research to better understand the nature of different source classes.

Additionally, there is currently a lack of dedicated research focused on ISs and an in-depth analysis of their specific properties compared to the main Seyfert types. Occasionally, IS objects can introduce ambiguity into samples of AGN classified as Seyferts. For example, a study in Ref. [20] reported on a NLS1, which exhibits a characteristic IS profile for Hβ, featuring a combination of broad and narrow components.

This interpretational challenge is closely tied to the quality of the spectra. When the S/N ratio is particularly low, a faint BLR emission, typical of Sy1.8/1.9, may mix with the continuum, giving the appearance of an Sy2. Conversely, a faint NLR emission, typical of Sy1.2, can be overwhelmed by the broad component, resulting in an Sy1-like line shape for the Balmer lines. To address this ambiguity, one potential solution is to prioritize the study of high-S/N spectra, ensuring more accurate classifications. However, this approach may necessitate excluding fainter sources or observations from small telescopes. As always, a balance must be struck between the completeness of the samples and the precision of our results.

The study in the current paper is centered on the analysis of the optical spectra of the selected sources, while the analysis of the X-ray spectra of the same sample will be included in a forthcoming paper. Here are presented only first results of this study; error estimation is not present, but as a reference we calculate it for the worst spectra in the sample (lower S/N), which is CGCG (Catalogue of Galaxies and of Clusters of Galaxies) 164–019. In this case, we adopted Hβ as representative for the other lines. The error is calculated producing 100 spectra summing the original one with a random noise proportional to the one between 5050–5150 Å and performing again the fitting obtaining a distribution for the curve parameters (amplitude, wavelength, width). The errors on the fitting parameters do not exceed 10%.

The paper is organized as follows. Section 2 describes sample selection procedure, while Section 3 describes the spectral analysis applied here. Section 4 contains the results of the BPT/VO (Baldwin–Phillips–Terlevich/Veilleux–Osterbrock) diagrams, and Section 5 gives the line ratios obtained. Section 6 conncludes on the study.

In this paper, we assume standard ΛCDM (cold dark matter with cosmological constant, Λ) cosmology, with the day Hubble expansion rate, $H_0 = 73.3$ km s^{-1} Mpc^{-1}, the Universe matter density, $\Omega_{matter} = 0.3$, and the vacuum energy density, $\Omega_{vacuum} = 0.7$ [21].

2. Sample Selection

To obtain a reliable sample of Seyfert galaxies, we selected two complementary samples using their BASS (Swift-BAT AGN Spectroscopic Survey) or SDSS (Sloan Digital Sky Survey) spectra, thus relying on their optical emission properties. The first sample, obtained from the BASS [22], comprises hard-X-ray-selected sources. Hard-X-ray emission primarily originates from the corona of the accretion flow, interacting with cold material through the inverse Compton scattering of optical/UV (ultra-violet) photons on relativistic

electrons [23]. At the same time, soft X-ray are absorbed by neutral hydrogen, hardening the spectrum. Consequently, according to the UM, these sources tend to be biased toward high viewing angles, such as almost edge-on orientations.

The second group of Seyfert galaxies was selected from the study [14] and is a γ-ray-selected sample from the 4th Fermi Large Area Telescope catalog (4FGL) [24]. γ-ray emission is closely related to the only AGN components capable of producing these energetic photons: the relativistic jets. In the UM framework, these objects are biased toward small viewing angles, resembling face-on orientations, with relativistic jets being almost aligned with the observer's line of sight. Our study involves the objects from Ref. [14] labeled as SEY (Seyferts), MIS (misaligned), CL (changing-look), NLS1, and AMB (ambiguous).

These selected samples complement each other due to the different selection methods: the first sample prefers edge-on sources, often associated with Sy2 or high–intermediate types (Sy1.8/1.9), while the second one favors face-on galaxies that can be identified as Sy1 or low–intermediate types (Sy1.2/1.5).

Following the preliminary selection (see the second row in Table 2), all spectra were meticulously inspected one by one and categorized into partial and complete samples. The first group includes sources where only Hβ and [O III]$\lambda\lambda$4959, 5007 were visible, while the second group encompasses sources with a spectral range from Hβ to [S II]$\lambda\lambda$6717, 6731, which is ideal for constructing the BPT/VO diagrams [25,26]. These diagrams can distinguish between starburst objects and AGN, as well as classify AGN into Seyfert and low-ionization nuclear emission-line region galaxies (LINERs) [27]. These digrams rely on the ratio between Balmer lines and ionized forbidden lines, revealing the presence of a more or less powerful radiation field, which, in turn, is related to the presence or absence of a central emitting region, the AGN.

Table 2. Selection steps operated to obtain the final sample using the BASS and SDSS optical spectra of the sources. See text for details.

4FGL		BASS	
Number	**Condition**	**Number**	**Condition**
2982	Total number of sources from 4FGL (with 1H 0323+342 and PKS 2004-447)	1210	Total number of sources from BASS
80	CL + MIS + SEY + NLS1 + AMB	638	With the optical spectra
52	With at least some spectral features visible (Hα/Hβ/[O III])	334	With at least some spectral features visible (Hα/Hβ/[O III])
15	Complete spectra (from Hβ to [S II])	121	Complete spectra (from Hβ to [S II])
11	No Sy1.9, [O I]λ6300 and/or [S II]$\lambda\lambda$6717, 6731 significant	38	No Sy1.9, [O I]λ6300 and/or [S II]$\lambda\lambda$6717, 6731 significant

As an initial approach, we only considered the complete spectra, enabling us to construct the BPT/VO diagrams. At this point, the two samples consisted of 121 sources from the BASS selection and 50 objects from the 4FGL selection.

We excluded Sy1.9 sources from the sample due to the Balmer decrement calculation, which relies on the ratio between the broad components of both Hα and Hβ, a feature absent in Sy1.9 (only present in Hα). Consequently, we obtained 38 AGN from BASS and 9 sources from 4FGL. A summary of these steps is provided in Table 2.

The limited number of sources in the 4FGL sample results from our reliance on publicly available spectra from the SDSS. We supplemented our dataset with two additional objects from the 4FGL sample, namely, 1H 0323+342 and PKS 2004-447, both NLS1 sources. These spectra come from the Boller and Chivens spectrograph mounted on the Galileo telescope

in Asiago (University of Padova) and from FOcal Reducer/low dispersion Spectrograph 2 (FORS2) at the Unit Telescope UT1 (Very Large Telescope, European Southern Observatory), respectively. These spectra were added to provide a reference for the NLS1 group in terms of obscuration, Seyfert type, and disk luminosity. Both of the added spectra respect the same conditions for spectra selection, even if 1H 0323+342 shows quite faint [S II]$\lambda\lambda$6717, 6731 lines.

3. Spectral Analysis

3.1. Preliminary Steps

The spectral analysis followed the classical initial steps, including cosmological redshift correction, de-reddening, host galaxy subtraction, and iron line subtraction. Each of these steps was implemented using Python 3.0 scripts, and the specific tools used in each step are detailed below.

For cosmological redshift correction, we utilized a built-in function available in GitHub [28].

The de-reddening procedure was based on the Cardelli–Clayton–Mathis (CCM) extinction law [29] and the relationship between $A(V)$ (total extinction in magnitudes) and N_H (column density of neutral hydrogen atoms in cm^{-2}) [30]. To calculate N_H, we used the dedicated NASA-HEASARC tool [31], which provides a weighted value. We then converted this value into $A(V)$ using the proportionality factor of 5.3×10^{22} mag cm^{-2} and applied it within the CCM extinction law,

$$I_{\lambda,0} = I_\lambda \times 10^{0.4 \times A(\lambda)}. \tag{3}$$

for the intensity, where λ is the wavelength, and $A(\lambda)$ is the generalized version of $A(V)$.

Host galaxy subtraction was carried out exclusively for sources with the redshift, $z \lesssim 0.3$ [32], and it was applied to spectra where the absorption features were well distinguishable. We employed galaxy templates from Ref. [33], which encompass various host galaxy types, including elliptical and spiral galaxies, with a spectral resolution of 5 Å. Due to the template's inherent wavelength binning, we needed to re-bin the AGN+host spectra before conducting the subtraction. In general, we used the Ca II lines at 3934 Å and 3968 Å as references to renormalize the template. These lines are exclusively produced by the galaxy's stellar components.

For the iron subtraction, we made use of templates from Refs. [34,35], which are accessible on the Serbian Virtual Observatory website [36]. These templates span the wavelength range from 4000 Å to 5500 Å and include various Doppler widths of Fe II lines, ranging from 700 to 2800 km s^{-1}. We performed iron subtraction in spectra where the peaks at 4 570 Å and 5270 Å exceeded the continuum value by at least 2σ (standard deviation).

3.2. Line Fitting

Similar to the iron subtraction, line fitting was performed with a detection limit set above 2σ. This constraint contributed to the limitation in the number of sources analyzed. This procedure proved especially useful in cases where the considered line was quite faint and closely intertwined with noise contributions to the flux.

To construct the BPT/VO diagram, we employed a multi-Gaussian model for fitting the following lines: Hβ, [O III]$\lambda\lambda$4959, 5007, [O I]λ6300, [N II]$\lambda\lambda$6548, 6583, Hα, and [S II]$\lambda\lambda$6717, 6731. We chose the multi-Gaussian approach due to the composite nature of the spectra, as previously mentioned, which include both a broad emission component and a narrow emission component (BLR and NLR, respectively). The narrow peaks of Hβ and Hα occur in the same region as the forbidden lines (e.g., [O III]). Consequently, the full-width-at-half-maximum (FWHM) of these lines remains fixed, limiting the number of free parameters. An alternative to Gaussian fitting is the Lorentzian approach, but it does not adequately fit the composite profile of these spectra. Specifically, it can overestimate the contribution of the wings when the narrow component dominates or overestimate the peak when the broad component is prominent. A comparison between the multi-Gaussian and Lorentzian approaches is illustrated in Figure 1. However, selecting the correct model is

not always straightforward, as seen in Figure 2, where a double Gaussian and a Lorentzian yield similar profiles when the FWHM is approximately 2000 km s^{-1}. This is particularly relevant, because 2000 km s^{-1} marks the boundary between classifying an object as an NLS1 or an Sy1. The ability to distinguish between these two classes is highly dependent on the resolution of the analyzed spectra, as emphasized in Ref. [20].
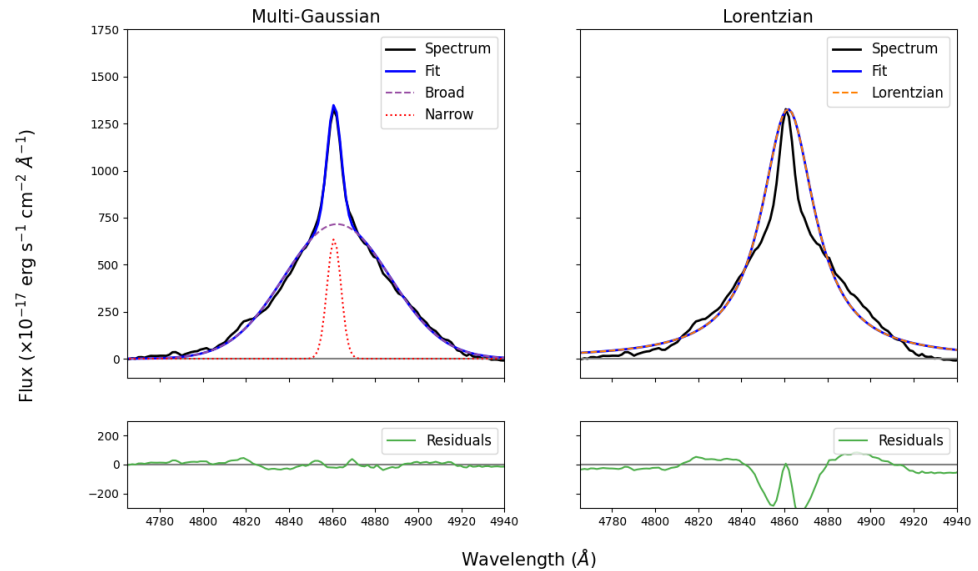

Figure 1. Comparison of Hβ fitting for Mrk 79. **Left:** a multi-Gaussian approach is used, with a curve for BLR emission (dashed violet line) and a second curve for the NLR one (dotted red line); the sum of the two components is shown in blue. **Bottom:** the residuals (in green) representing the difference between the adopted model and the spectra. **Right:** the same analysis but conducted with a Lorentzian approach. One can see that in the Lorentzian case, the residuals are more pronounced and tend to overestimate both the center and the wings of the line. See text for details.
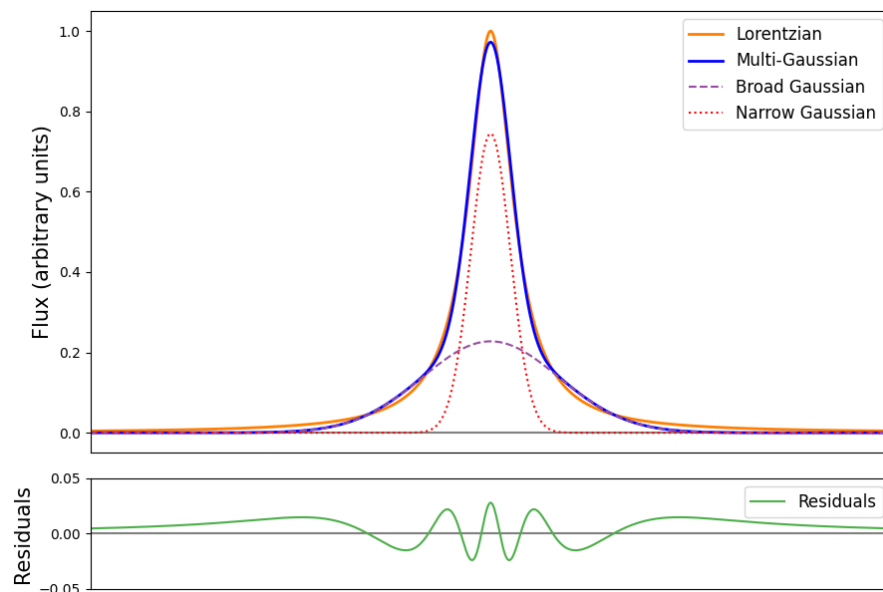
Figure 2. **Top** comparison between a Lorentzian profile (orange) and a multi-Gaussian one (blue), with the narrow (red) and broad (violet) components with an FWHM of approximately 2000 km s^{-1}. **Bottom**: the residuals as the difference between the double-Gaussian model and the Lorentzian profile. See text for details.

To minimize the number of free parameters in the fitting process, we imposed some constraints. For instance, starting with the [O III]$\lambda\lambda$4959, 5007 lines, we allowed the most prominent line ([O III]λ5007) to be fitted freely while binding all the parameters (center, FWHM, and amplitude) of the other line. The center displacement and FWHM were the same for both lines, and the amplitude of [O III]λ4959 was fixed at one-third of the amplitude of [O III]λ5007 [37]. Similar FWHM constraints were applied between [O III], and the narrow component of Hβ and Hα. When dealing with the Hα+[N II] complex, constraints were applied to the amplitudes of the two nitrogen lines and the FWHM. The amplitude ratio between [N II]λ6548 and [N II]λ6583 was set to 1/2.96 [38] (see NIST database [39]), and the FWHM was kept consistent with the previous cases. The same procedure was employed for the [S II]$\lambda\lambda$6717, 6731 lines, where the FWHM was identical for both lines. An example of line fitting using this procedure is depicted in Figure 3. The fitting process was conducted using dedicated Python code based on the Levenberg–Marquardt algorithm [40] and least squares statistics.
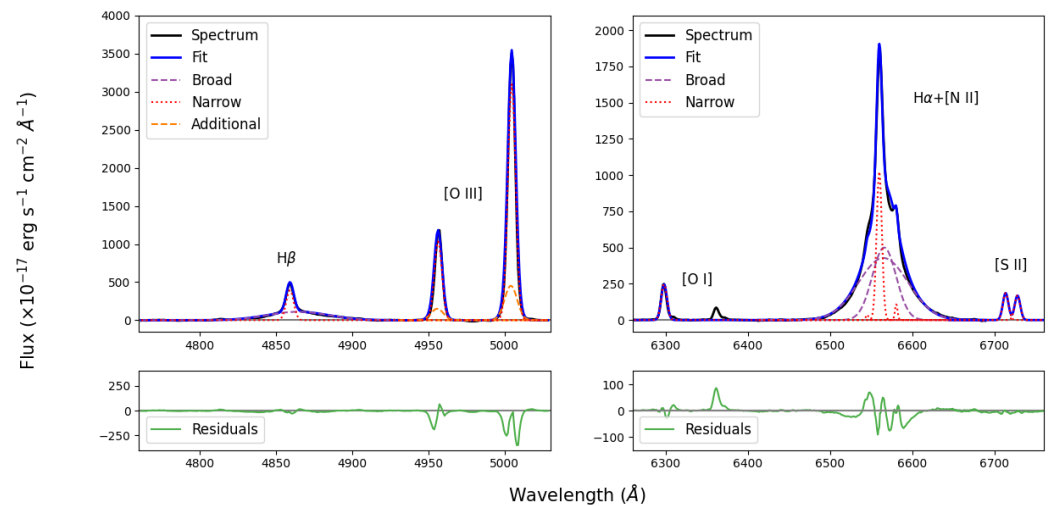

Figure 3. Left to **right**: fitting of Hβ; [O III]$\lambda\lambda$4959, 5007; [O I]λ6300; Hα; [N II]$\lambda\lambda$6548, 6583; [S II]$\lambda\lambda$6717, 6731 for Mrk 110 as indicated. As in Figure 2, the blue line represents the total fitting, the dotted red curves represent the narrow component, th dashed violet curves represent the broad component(s), and the dashed orange curve is associated with a possible outflow component related to [O III] emission. The blueshifted bumps are commonly observed in [O III] profiles [41]. **Bottom:** the residuals shown in light green; the [O I]λ6363 line (**bottom, right**) is present as a residual because it was not fitted during the analysis.

3.3. Notes on the Sample

As stated at the beginning of Section 3.2, some spectra were not considered in the sample due to the faintness of the lines, in particular [O I]λ6300 and [S II]$\lambda\lambda$6717, 6731. The 2σ criterion, together with the necessity of using the same sources in all the plots, further reduced the number of objects. In the end, we obtained 9 AGN from the 4FGL sample with SDSS and 38 sources from the BASS one. We also added two jetted NLS1 from 4FGL with other optical spectra: 1H 0323+342 and PKS 2004-447. From the BASS sample, we noticed three jetted AGN, 4C +29.30, 3C 227, and 3C 234.0, and five objects with parsec-scale jets, 2MASX J04234080+0408017 [42], Mrk 590 [43], NGC 985 [44], Mrk 110 [45], and Mrk 705 [45]. It is important to notice that there is no superposition between the two samples.

For the spectra of 1H 0323+342, it is important to stress that this source was monitored by one of us (M.B.) between 2014 and 2021 with the Asiago Galileo telescope, and so a lot of spectra were available. To increase the S/N, we combined some of them, applied the same steps listed above (de-reddening, cosmological redshift, and iron subtraction),

and performed line fitting. The result is shown in Figure 4: both [O I]λ6300 and [S II]$\lambda\lambda$6717, 6731 are quite faint.
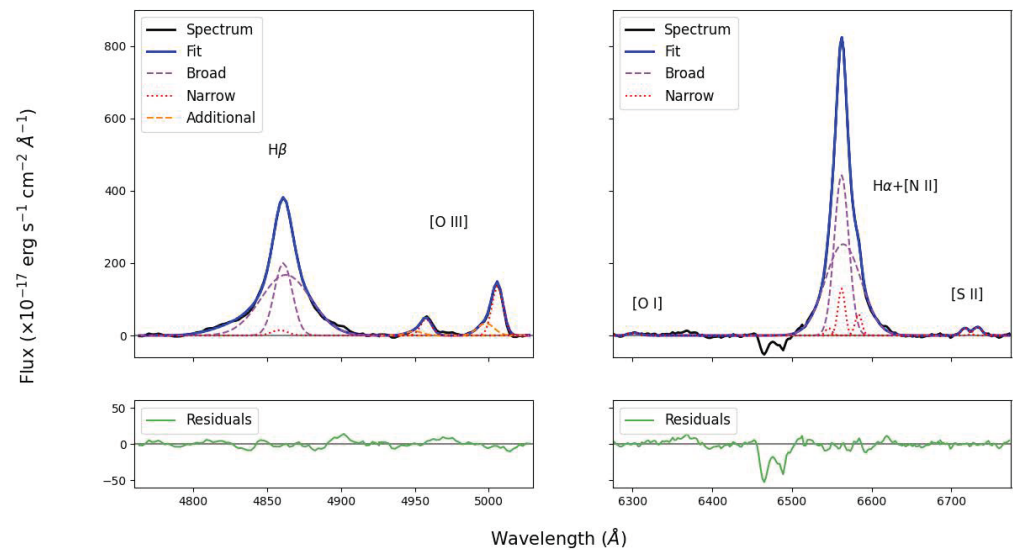
Figure 4. Fitting of the spectrum of 1H 0323+342 in the Hβ–[O III]$\lambda\lambda$4959, 5007 region (**left**) and that of the [O I]λ6300–[S II]$\lambda\lambda$6717, 6731 region for 1H 0323+432 (**right**). The lines are as in Figure 3. Additionally, there is a telluric absorption feature between 6450 Å and 6500 Å.

4. BPT/VO Diagrams

The BPT/VO diagrams are employed as a tool for the separation between AGN and starburst galaxies using the properties of different ionization lines. Many authors have proposed slightly different classifications [46,47], but they always identify three regions: starbursts, Seyferts, and LINERs. These separations can be seen in Figure 5 with solid and dotted lines. The dashed–dotted lines represent the limits for the sources in Ref. [48], which are spread in the upper-right part of the curve. Ref. [48] studied the optical properties of a homogeneous sample of the 3CR radio sources with redshift below 0.3. Consequently, this population characterizes the mean characteristics of jetted sources. Certainly, this dashed–dotted line serves as a rough reference used to compare a pure jetted sample with ours.

In Figure 5, most right, the line ratio index (LRI) vs. [O III]/Hβ, is also sourced from Ref. [48] and represents a composite view of the three BPT/VO diagrams. The *y*-axis aligns with the diagnostic diagrams, while the *x*-axis is calculated as follows:

$$\text{LRI} = \frac{1}{3}\left(\log\frac{[\text{N II}]}{\text{H}\alpha} + \log\frac{[\text{S II}]}{\text{H}\alpha} + \log\frac{[\text{O I}]}{\text{H}\alpha} \right). \tag{4}$$

The objective here is to create a more stable index than single-line ratios, aimed at avoiding ambiguous classifications, as emphasized in Ref. [47]. In the LRI-log([O III]/Hβ) plot, two distinct regions are separated by a horizontal line at about 1: the high-Excitation-Index (EI) and low-EI regions. The EI represents the overall ratio of high- and low-excitation emission lines in each source. While these two populations are well visible in Ref. [48], the current study primarily focuses on sources concentrated in the high-ionization region. The absence of low-ionization sources may be related to the nature of the selected sources (AGN) and the methods used to obtain the sample, based on γ- and hard-X-emissions.

From Figure 5, one can immediately see that the majority of the sample falls within the Seyfert region, with some exceptions in the LINER region. Particularly, objects in the LINER area can be interpreted as AGN undergoing a transition from an efficient phase to an inefficient phase in the accretion process [47], possibly nearing the end of an activity phase. The two starburst sources in the first BPT/VO diagram are PKS 2335+03 (located close to

the boundary) and 3C 227 (outlying in all three BPT/VO diagrams). The first spectrum is low-resolution, while the second one presents a complicated structure, especially for the permitted lines (see Figure A1 in Appendix A).

We also explored the possibility of replacing line fluxes with peak values to address modeling issues, but this did not prove to be a valid alternative. For further details, see Appendix B.
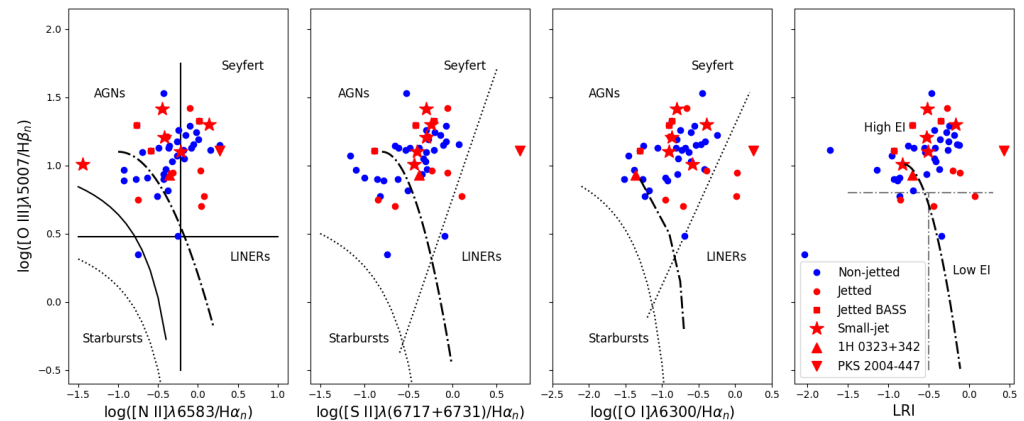
Figure 5. The three plots on the left represent the BPT/VO diagrams for the selected sources, and the one on the most right is from Ref. [48] and uses the LRI. In blue, the non-jetted objects (BASS), and in red, the jetted ones (mainly 4FGL, some BASS objects). The jetted sources are marked with different symbols according to their properties: the red dots are the classical jetted AGN , the red squares are from BASS ; the red stars present small jets in the parsec scale, and the triangles show 1H 0323+432 and PKS 2004-447. The solid lines identify the classification limits according to Ref. [46], the dotted lines, those according to Ref. [47], and the dashed–dotted lines (both black and gray ones), those according to Ref. [48]. See text for details.

5. Line Ratios

The objective is to investigate the relationship between the intrinsic properties of AGN and obscuration. Oxygen luminosity ($L_{[O\,III]}$) can be interpreted as a proxy for disk luminosity (L_{disk}) [49–51]. Some authors criticized this statement [52,53], demonstrating that in some cases, [O III] is also partially obscured in type 2 AGN, so it is not totally independent from the classification type of the source. In the optical range, [O III] luminosity is the sole quantity that we can use as a tool for the disk one. Expanding the analysis to X-rays, we can eliminate this problem, producing more accurate conclusions. With this aim, we also analyze the X-ray part of the spectra of the same objects to obtain more solid information about the possible connection between disk luminosity and classification [54].

To assess obscuration, we utilize the Balmer decrement and Seyfert type as tools. The Balmer decrement is frequently employed as a means to assess the degree of obscuration, because its intrinsic value remains relatively insensitive to variations in gas temperature and density within the region being examined. However, the total value, which is what one observes, includes the effects of obscuration. For case B recombination in HII regions, the reference value for $H\alpha/H\beta$ is about 2.9 [55]. In contrast, for AGN, this theoretical value can vary depending on the Seyfert type, as emphasized by various authors [56–58]. Consequently, if one aims to disentangle the level of obscuration from the overall $H\alpha/H\beta$ ratio, one to require a reliable estimate of the intrinsic value. This task is particularly challenging when the sample comprises different Seyfert types. Focusing the study on unobscured AGN, such as Sy1, some researchers [59,60] have discovered a general consensus between the Balmer decrement values and case B recombination. The values typically fall within the 3.0–3.5 range, with a dispersion of 0.2–0.6. There are, however, some outliers with decrements of 1.6 or 7.8. Consequently, we consider case B recombination as a valid reference, though it is important to bear in mind that the conclusions regarding the

Balmer decrement should account for the Seyfert classification. Furthermore, it is worth noting that the intrinsic value may be higher than the commonly used value of 2.9.

The link between $L_{[O\ III]}$ and L_{disk} arises from the level of activity of the central engine and the degree of ionization produced in the NLR. Additionally, the stellar component of the host galaxy can contribute to the oxygen flux, particularly when the orientations of the host and AGN are not aligned [61]. This different inclination between the host and the AGN was studied in Refs. [62,63], concluding that the difference in viewing angle from the central engine (using the radio-jet orientation) between Sy1 and Sy2 is a direct and independent confirmation of the UM. Some explanations for this misalignment can be the warping of the accretion disk due to self-irradiation instabilities or the presence of a second gravitating system as during a merger. This does not apply to the case considered here, because the systems in question are not experiencing significant instabilities, except for UGC 8327, which is a dual system.

The inclusion of X-ray spectral analysis provides an independent measure of obscuration. This method can help us disentangle the influence of Seyfert types on the Balmer decrement and address any of the host galaxy–AGN misalignment issues discussed just above.

For the moment, we generated three plots, shown in Figure 6, which are discussed in what follows.

5.1. Seyfert Type versus Balmer Decrement

The initial approach was to compare the Seyfert type with the BLR Balmer decrement (Hα/Hβ). Hα/Hβ provides an estimate of the extinction level, because the decrement value is closely related to gas physical properties. Consequently, discrepancies with respect to the theoretical value can be attributed to obscuration effects, even if some authors argue this choice [56–58]. In Figure 6, left, the results are displayed: the non-jetted and jetted populations do not exhibit a noticeable separation. This suggests that there are no significant differences in terms of the Balmer decrement and classification. This result poses an interpretative challenge.
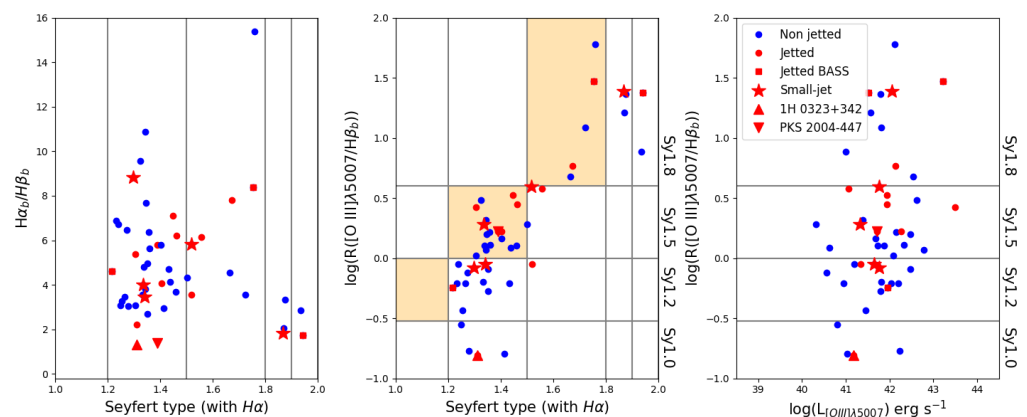
Figure 6. Line ratios for the sample considered; the markers are the same as in Figure 5. The colored areas represent the correspondence between the two Seyfert classification methods adopted (from [O III]/Hβ and Hα components). The solid gray lines show the separations among the Seyfert classes. The two plots on the right share the same *y*-axis. and identify the same Seyfert sub-classes indicated between the diagrams.

The Balmer decrement is commonly used as an indicator of obscuration, with Sy1/Sy1.2/ Sy1.5 being expected to be less obscured (lower Balmer decrements) than Sy2/Sy1.9/Sy1.8 (higher Balmer decrements). If the separation between jetted/non-jetted follows the UM scheme and, consequently, corresponds to face-on/edge-on sources (e.g., Sy1/Sy2), the Balmer decrement should display an ascending trend in Figure 6, middle, which is not observed. The results of the statistical tests are as follows: Spearman: $r_p = -0.10$,

p-value = 0.46; Pearson: $r_p = -0.07$, *p*-value = 0.61; and Kendall: $r_k = -0.06$, *p*-value = 0.53). In this case, there is no apparent correlation.

One of possible explanations for the lack of a correlation between the Balmer decrement and the Seyfert type can be the dependence of $H\alpha/H\beta$ on the radiation field properties. In this context, we can have an excess of $H\alpha$-emission relative to $H\beta$ produced by an intense source of high-energy radiation (the AGN) [64].

Another point to stress is the possible bias introduced by the lack of Sy1.9 sources in the sample; for these objects, it is not possible to calculate $H\alpha_b/H\beta_b$ due to the missing broad component in $H\alpha$. From Figure 6, left, one can see some objects in the Sy1.9 region: this is due to the classification method adopted. As explained in Section 5.2, [O III]/$H\beta$ traces the Seyfert type better than $H\alpha$.

Finally, the influence of the Seyfert type on the intrinsic value of the Balmer decrement can also play a role, as stated in just above.

5.2. Seyfert Type versus [O III]/Hβ

A second approach involved comparing different Seyfert classification methods. In Figure 6, middle, one can see that the two methods generally agree. For visual clarity, we identify the colored areas as regions where the two classification methods coincide. Almost all the data points are distributed around the diagonal, differing by at most one Seyfert class along both axes. In particular, objects categorized as Sy1/1.2 on the *y*-axis exhibit a tendency to be "over-classified" on the *x*-axis, indicating higher Seyfert types. For example, 1H 0323+342, a commonly recognized NLS1, is classified as a Sy1 based on [O III]/$H\beta$ measurements, but as a Sy1.2/1.5 when considering $H\alpha$ properties. While the difference is not extreme, it is notable. This implies that the $H\alpha$-based classification method may not be as reliable as the [O III]–$H\beta$ approach, especially for lower Seyfert types. The issue with the $H\alpha$ method may stem from challenges in accurately fitting the $H\alpha$+[N II] complex or from intrinsic characteristics of the BLR.

Statistical tests revealed a trend without a correlation: Spearman: $r_p = 0.77$, *p*-value = 3.57×10^{-10}, Pearson: $r_p = 0.85$, *p*-value = 5.77×10^{-14}, and Kendall: $r_k = 0.59$, *p*-value = 6.44×10^{-9}.

An important point to stress is the absence of separation on the horizontal axis between jetted and non-jetted AGN. The sample studied here, is based on 4FGL and BASS objects, so the jetted sources are selected using the high-energy part of the spectrum. Keeping this in mind, according to the UM, this type of jetted sources should be biased towards lower IS types (such as Sy1.2/1.5), and non-jetted ones, towards higher types (such as Sy1.8/1.9). However, this is not visible in Figure 6.

Globally, [O III]/$H\beta$ shows a trend with the Seyfert type (with $H\alpha$), see Figure 6, middle. In the UM framework, an increasing Seyfert type is interpreted as indicating a higher level of obscuration (from Sy1 to Sy2). Consequently, we adopt [O III]/$H\beta$ as a proxy for the obscuration level. No same correspondence is observed for the Balmer decrement.

5.3. $L_{[O\ III]}$ versus [O III]/Hβ

The final relationship we investigated was that between oxygen luminosity ($L_{[O\ III]}$) and [O III]λ5007/$H\beta$. As mentioned just above $L_{[O\ III]}$ serves as a tool for intrinsic properties, particularly disk luminosity, while the obscuration level is better estimated using [O III]/$H\beta$. The pros and cons of these quantities were discussed in the begining of Section 5; here, we assume that both well trace the intrinsic and obscuration properties of the selected AGN.

The results from Figure 6, right, reveal that the two properties are not related. No significant correlation is observed in this comparison, and the two populations are mixed. This suggests that the Seyfert type (and subtype) does not depend on $L_{[O\ III]}$ and, consequently, the intrinsic properties that can be derived from the optical range of the spectrum. In other words, this implies that the properties of the central region of the AGN do not lead to differences in terms of Seyfert type, supporting the idea of a common structure,

as predicted by the UM. The results of the statistical tests are as follows: Spearman: $r_p = 0.22$, p-value = 0.13, Pearson: $r_p = 0.26$, p-value = 0.08, and Kendall: $r_k = 0.15$, p-value = 0.15.

6. Conclusions and Future Work

We conducted a search for a possible relationship between the intrinsic properties and obscuration of a sample of Seyfert galaxies, categorized as jetted and non-jetted sources. Confirming their classification as AGN, particularly as Seyfert for the majority, was achieved using the BPT/VO diagram. Objects situated within the LINER region can be interpreted as aging AGN in their final activity phase. Additionally, we created the LRI-[O III]/Hβ plot, where nearly all the data points fall within the high-EI region. This trend likely stems from the nature of the sources (AGN) and the spectral bands used for sample selection.

Next, we generated line ratio plots with the initial aim of finding a suitable parameter related to the obscuration level. Our first attempt, using the Balmer decrement, did not yield significant results. However, in a subsequent analysis, we employed [O III]/Hβ, which provided valuable insights when compared with the Seyfert type, as expected from the UM. As for intrinsic properties, optical spectroscopy limits us to using $L_{[O\ III]}$, which can be an indicator of disk luminosity and, in turn, depends on the central engine's activity. A comparison of these two parameters did not reveal a significant relationship, suggesting that the central engine's structure in Seyfert galaxies may be consistent across all types, with obscuration remaining the most plausible explanation. Summarizing, we did not find any well-indicated separation between jetted/non-jetted sources in terms of the considered parameters; this finding aligns with the UM.

On the contrary, no clear enough separation between jetted and non-jetted objects in terms of IS sub-type was found. In Figure 6, middle, shows no a pronounced distinction between Sy1.2/1.5 and Sy1.8/1.9, based on γ-ray jetted/non-jetted categorization. This implies that jetted sources do not always correspond to lower Seyfert sub-types (such as Sy1.2 and Sy1.5) but can happen to correspond to Sy1.8/1.9. This unpredicted result challenges the UM and warrants further investigation.

One of potential future steps would involve incorporating X-ray analysis of the same sources to calculate the parameter N_H. Combining optical and X-ray analyses allows for the use of the low-energy part as an estimator of obscuration (using [O III]/Hβ or the Balmer decrement) and the high-energy component as a more robust indicator of accretion power.

Another approach is to focus the analysis on specific sources, utilizing integral field spectra. Data cubes enable the study of each region of the AGN, providing both spectra and photometry simultaneously.

Appendix A

The fitting procedure for 3C 227, showing the presence of multiple bumps and components in the permitted lines, is here presented.
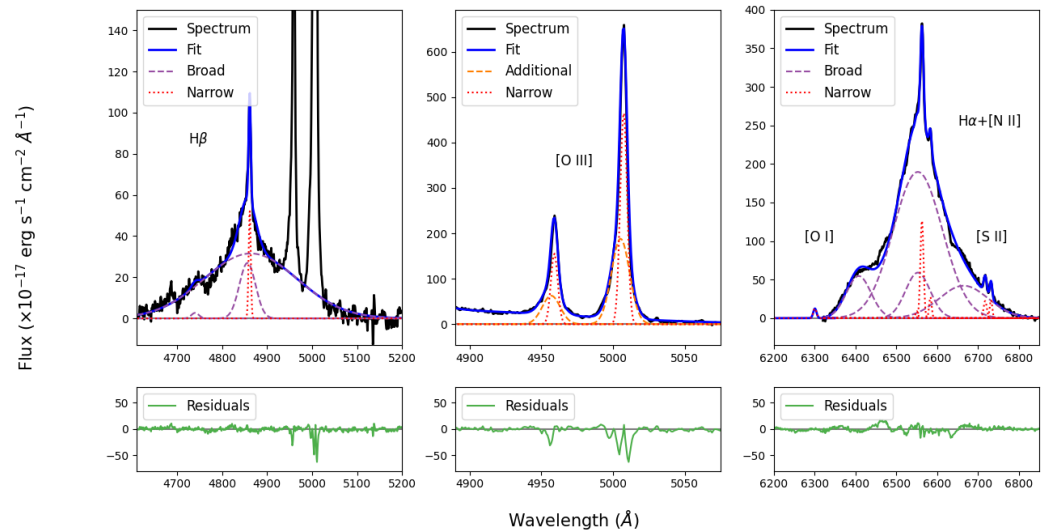
Figure A1. Line fitting of the Hβ–[O III]$\lambda\lambda$4959, 5007 region (**left** and **middle**) and of the [O I]λ6300–[S II]$\lambda\lambda$6717, 6731 region (**right**) for 3C 227. The line styles are the same as in Figure 2.

Appendix B

Here, we present the results of the BPT/VO diagrams calculated using the value of the peak of the lines, instead of the flux. This arises from the potential to avoid the fitting procedure when the spectrum has a low S/N by estimating only the value of the maximum flux for each line. The results are depicted in Figure A2. When comparing these results with those shown in Figure 5, a significant difference is evident between the two approaches. To assess this, we calculated the average shifting of the points in both the vertical and horizontal axes to determine if there was a common trend and if applying a correcting factor was warranted. The average shift (in both axes) and the standard deviation are of a similar order of magnitude, as indicated in Table A1. Consequently, one can conclude that there is no preferential shift in the positions between the classical BPT/VO and the line-peak BPT/VO plots. The same observation applies to the LRI-log([O III]/Hβ) plot. This underscores the fundamental role of the fitting procedure in producing a valid classification of the sources.
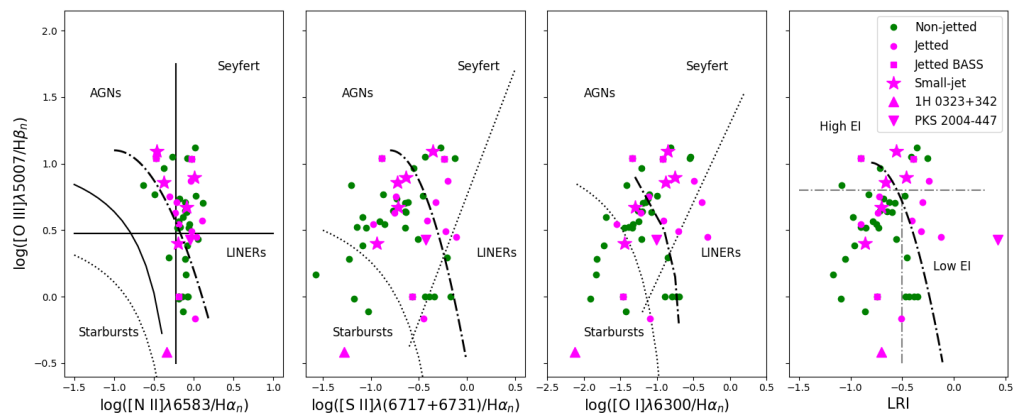
Figure A2. BPT/VO diagram of the here selected sample, utilizing the line peak instead of the flux. The line styles and symbols remain consistent with those in Figure 2, but different colors are employed to emphasize the distinct method employed here. The green points correspond to the blue ones (non-jetted), and the magenta points correspond to the red ones (jetted, small jets, and NLS1) in the previous BPT/VO diagram (Figure 5).

Table A1. Results of the horizontal and vertical shifts (with standard deviation) (σ) in the BPT/VO plots as difference between the peak (Figure A2) and the flux (Figure 5) cases.

	4FGL		**BASS**	
Axis	**Shift**	σ	**Shift**	σ
$\log([\text{N II}]/\text{H}\alpha)$	0.52	0.32	0.08	0.10
$\log([\text{S II}]/\text{H}\alpha)$	0.43	0.22	0.11	0.18
$\log([\text{O I}]/\text{H}\alpha)$	0.43	0.31	0.15	0.21
$\log([\text{O III}]/\text{H}\beta)$	0.63	0.32	0.19	0.57

Appendix C

Here, the complete list of the sources included in the study is presented. The list of the sources (Table A2) contains information for the BASS sample from Ref. [65]. Table A3 contains the list of the fluxes of the fitted lines used to produce the plots.

Table A2. List of sources. Here RA and DEC stay for the right ascension and the declination, respectively, z is the redshift and N_H is the galactic obscuration level. In the last row, the * symbol refers to the sum of six different spectra to produce the studied one: 2016-02-06, 2016-08-12, 2016-12-08, 2016-12-29, 2017-01-20, and 2017-12-18.

IAU Name	Alias	RA (° J2000)	DEC (° J200)	z (10^{-3})	N_H (10^{20} cm^{-2})	Telescope	Exposure (ks)	Date
				BASS				
J0149-5015	2MASX J01492228-5015073	27.34	−50.25	2.99	1.75	Palermo	1.20	2010-11-12
J0157+4715	2MASX J01571097+4715588	29.30	47.27	4.79	11.0	Perkins	2.40	2011-05-01
J0206-0017	Mrk 1018	31.57	−0.29	4.27	2.48	SDSS	2.70	2000-09-25
J0214-0046	Mrk 590	33.64	−767.00	2.63	2.77	SDSS	4.20	2003-01-10
J0234-0847	NGC 985	38.66	−8.79	4.30	3.48	Palomar	0.15	2013-08-13
J0238-4038	2MASX J02384897-4038377	39.70	−40.64	6.13	2.06	Palomar	0.15	2013-08-13
J0312+5029	2MASX J03120291+5029147	48.01	50.49	6.15	3.45	Perkins	2.40	2011-06-01
J0330+0538	2MASX J03305218+0538253	52.72	5.64	4.58	1.16	UH	1.22	2012-11-01
J0333+3718	2MASX J03331873+3718107	53.33	37.30	5.47	1.48	Masetti	1.80	2006-10-02
J0423+0408	2MASX J04234080+0408017	65.92	4.13	4.62	12.6	Palomar	0.15	2012-10-18
J0503+2300	LEDA 097068	75.74	23.00	5.81	23.4	Palermo	1.80	2009-01-29
J0605-2754	2MASX J06054896-2754398	91.45	−27.91	8.98	2.64	Masetti	1.00	2009-11-30
J0733+4555	1RXS J073308.7+455511	113.29	45.92	14.15	7.19	SDSS	3.30	2004-11-05
J0736+5846	Mrk 9	114.24	58.77	3.99	4.83	Palomar	0.15	2014-02-22
J0742+4948	Mrk 79	115.64	49.81	2.21	5.43	FAST	0.72	2005-12-29
J0752+1935	2MASX J07521780+1935423	118.07	19.60	11.70	4.06	SDSS	3.30	2003-10-27
J0803+0841	2MASX J08032736+0841523	120.86	8.70	4.68	2.87	SDSS	4.50	2007-02-08
J0804+0506	Mrk 1210	121.02	5.11	1.35	3.86	Palomar	0.15	2012-10-18
J0829+4154	2MASX J08294266+4154366	127.43	41.91	12.61	3.57	SDSS	3.50	2008-02-28
J0832+3707	FBQS J083225.3+370736	128.11	37.13	9.20	3.27	SDSS	5.10	2002-01-23
J0840+2949	4C +29.30	130.01	29.82	6.47	4.56	SDSS	22.89	2003-10-25
J0842+0759	2MASX J08420557+0759253	130.52	7.99	13.37	5.76	SDSS	2.24	2003-11-21
J0843+3549	2MASX J08434495+3549421	130.94	35.83	5.39	2.98	SDSS	2.10	2003-02-02
J0904+5536	2MASX J09043699+5536025	136.15	55.60	3.72	2.32	SDSS	9.00	2000-12-29
J0918+1619	Mrk 704	139.61	16.31	2.95	2.74	Palomar	0.15	2015-02-17
J0923+2255	MCG +04-22-042	140.93	22.91	3.30	3.60	Palomar	0.15	2015-02-17
J0925+5219	Mrk 110	141.30	52.29	3.52	1.27	SDSS	4.80	2006-01-05
J0926+1245	Mrk 705	141.51	12.73	2.86	3.43	SDSS	5.10	2006-12-23
J0935+2617	2MASX J09352707+2617093	143.86	26.29	12.21	1.56	SDSS	13.02	2005-12-28
J0942+2341	CGCG 122-055	145.52	23.69	2.13	2.42	SDSS	3.30	2005-12-31
J0945+0738	3C 227	146.94	7.42	8.60	2.00	SDSS	2.70	2003-03-27
J0959+1302	NGC 3080	149.98	13.04	3.54	2.74	SDSS	2.70	2004-02-20
J1001+2847	3C 234.0	150.46	28.79	18.48	1.62	SDSS	2.52	2009-04-17
J1023+1951	NGC 3227	155.88	19.87	0.33	1.86	FAST	0.33	2006-01-05
J1043+1105	SDSS J104326.47+110524.2	160.86	11.09	4.77	2.38	SDSS	3.90	2004-04-20
J1315+4424	UGC 08327	198.82	44.41	3.55	1.68	SDSS	1.92	2004-03-25
J1445+2702	CGCG 164-019	221.40	27.03	2.96	2.37	Palomar	0.15	2005-02-17
J1508-0011	Mrk 1393	227.22	−197.00	5.44	4.64	SDSS	2.70	2001-03-22

Table A2. *Cont.*

IAU Name	Alias	RA (° J2000)	DEC (° J200)	z (10^{-3})	N_H (10^{20} cm^{-2})	Telescope	Exposure (ks)	Date
				4FGL				
J0038-0207	3C 17	9.59	−2.13	22.04	2.48	SDSS	4.50	2014-12-21
J0316+4119	IC 310	49.18	41.32	1.90	11.5	SDSS	13.00	2003-12-03
J0324+3410	1H 0323+342	51.17	34.18	6.29	11.7	Asiago	1.20 (×6)	*
J0937+5008	GB6 J0937+5008	144.30	50.15	27.55	1.31	SDSS	3.60	2014-12-01
J0958+3224	3C 232	149.59	32.40	53.06	1.57	SDSS	2.70	2018-01-24
J1443+5201	3C 303	220.76	52.03	14.12	1.66	SDSS	2.10	2003-05-27
J1516+0015	PKS 1514+00	229.17	0.25	5.26	4.17	SDSS	4.50	2000-05-25
J2007-4434	PKS 2004-447	301.98	−44.58	24.00	2.97	VLT	0.15	2015-10-17
J2118+0013	PMN J2118+0013	319.57	0.22	46.28	5.87	SDSS	3.60	2017-10-13
J2118-0732	TXS 2116-077	319.72	−7.54	26.01	7.99	SDSS	2.70	2001-08-25
J2338+0326	PKS 2335+03	354.53	3.45	26.90	4.96	SDSS	2.70	2018-10-11

Table A3. List of fluxes. All the quantities refer to the flux of the listed line or component. All the terms are expressed in the logarithmic form (e.g., $\log_{10}(\mathrm{H}\beta_{\mathrm{tot}})$), and the units are erg s^{-1} cm^{-2}.

Name	Hβ_{tot}	Hβ_b	[O III]λ4959	[O III]λ5007	[O I]λ6300	[N II]λ6548	Hα_{tot}	Hα_b	[N II]λ6583	[S II]λ6717	[S II]λ6731
					BASS						
J0149-5015	−11.57	−11.59	−12.20	−11.72	−12.65	−12.71	−10.77	−10.78	−12.24	−12.41	−12.40
J0157+4715	−10.84	−10.87	−12.14	−11.66	−15.92	−11.77	−10.35	−10.40	−12.06	−12.28	−12.43
J0206-0017	−11.33	−11.36	−11.89	−11.41	−12.61	−12.27	−10.51	−10.53	−11.80	−12.46	−12.50
J0214-0046	−11.09	−11.13	−11.33	−10.84	−12.07	−12.06	−10.49	−10.51	−11.58	−12.23	−12.23
J0234-0847	−10.74	−10.76	−11.32	−10.84	−11.97	−12.00	−9.79	−9.81	−11.53	−11.71	−11.71
J0238-4038	−10.88	−10.91	−11.59	−11.10	−12.48	−12.64	−10.33	−10.36	−12.17	−12.83	−12.82
J0312+5029	−10.59	−10.66	−10.95	−10.46	−11.68	−11.80	−9.74	−9.77	−11.33	−11.51	−11.58
J0330+0538	−10.61	−10.79	−10.59	−10.11	−11.77	−11.79	−9.94	−10.13	−11.32	−11.78	−11.79
J0333+3718	−10.73	−10.75	−11.21	−10.73	−12.28	−13.02	−10.23	−10.24	−12.55	−12.12	−12.14
J0423+0408	−11.70	−11.99	−11.08	−10.60	−12.15	−12.27	−11.20	−11.72	−11.80	−11.93	−11.97
J0503+2300	−10.26	−10.31	−10.88	−10.40	−11.97	−11.97	−9.58	−9.61	−11.49	−11.63	−11.63
J0605-2754	−11.27	−11.32	−11.59	−11.11	−12.23	−12.77	−10.48	−10.50	−12.30	−12.16	−12.24
J0733+4555	−10.68	−10.69	−11.94	−11.46	−13.03	−12.31	−10.18	−10.20	−11.84	−13.04	−13.03
J0736+5846	−10.63	−10.64	−11.56	−11.07	−12.66	−12.44	−10.11	−10.13	−11.96	−12.49	−12.53
J0742+4948	−10.31	−10.35	−10.76	−10.27	−11.62	−11.49	−9.67	−9.69	−11.02	−11.45	−11.51
J0752+1935	−10.77	−10.80	−11.21	−10.73	−11.76	−12.09	−10.19	−10.22	−11.61	−11.68	−11.78

Table A3. *Cont.*

Name	Hβ$_\text{tot}$	Hβ$_b$	[O III]λ4959	[O III]λ5007	[O I]λ6300	[N II]λ6548	Hα$_{tot}$	Hα$_b$	[N II]λ6583	[S II]λ6717	[S II]λ6731
J0803+0841	−11.54	−11.61	−11.78	−11.29	−12.30	−12.50	−10.55	−10.58	−12.03	−12.29	−12.34
J0804+0506	−11.05	−11.22	−10.49	−10.01	−10.98	−11.44	−10.38	−10.91	−10.96	−11.40	−11.32
J0829+4154	−11.31	−11.36	−11.73	−11.25	−12.11	−12.57	−10.58	−10.61	−12.10	−12.3	−12.26
J0832+3707	−10.62	−10.89	−11.58	−11.09	−12.37	−12.26	−10.33	−10.35	−11.78	−12.27	−12.27
J0840+2949	−12.50	−12.83	−11.93	−11.45	−12.66	−12.26	−11.73	−12.59	−11.78	−12.26	−12.37
J0842+0759	−11.42	−11.49	−11.49	−11.01	−11.95	−12.33	−10.48	−10.51	−11.86	−12.09	−12.22
J0843+3549	−12.02	−12.36	−11.48	−11.00	−11.99	−12.0	−11.29	−11.84	−11.53	−11.78	−11.83
J0904+5536	−11.28	−11.32	−12.01	−11.53	−12.67	−12.35	−10.59	−10.64	−11.88	−12.28	−12.34
J0918+1619	−10.16	−10.19	−10.94	−10.46	−12.38	−11.83	−9.72	−9.75	−11.35	−11.97	−12.05
J0923+2255	−10.52	−10.60	−10.98	−10.50	−12.04	−12.38	−9.95	−9.98	−11.90	−11.92	−11.95
J0925+5219	−11.11	−11.26	−11.14	−10.66	−11.70	−13.03	−10.24	−10.30	−12.56	−11.83	−11.87
J0926+1245	−10.51	−10.54	−11.07	−10.59	−12.05	−11.83	−9.97	−10.00	−11.36	−11.84	−11.85
J0935+2617	−11.28	−11.30	−11.99	−11.51	−12.71	−12.99	−10.45	−10.46	−12.52	−12.77	−12.86
J0942+2341	−11.41	−11.45	−11.85	−11.37	−12.47	−12.23	−10.77	−10.83	−11.76	−12.35	−12.34
J0945+0738	−10.75	−11.02	−11.75	−11.27	−12.92	−13.18	−10.35	−10.36	−12.71	−12.68	−12.77
J0959+1302	−11.07	−11.08	−12.45	−11.63	−16.52	−12.73	−10.57	−10.58	−12.26	−12.95	−12.88
J1001+2847	−11.68	−12.20	−11.21	−10.73	−12.60	−12.36	−10.98	−11.28	−11.88	−12.48	−12.47
J1023+1951	−10.24	−10.30	−10.50	−10.02	−11.06	−10.91	−9.51	−9.54	−10.44	−10.84	−10.85
J1043+1105	−11.11	−11.18	−11.50	−11.02	−12.29	−12.77	−10.37	−10.42	−12.29	−12.41	−12.48
J1315+4424	−11.75	−12.3	−11.90	−11.42	−11.79	−11.63	−11.03	−11.85	−11.35	−11.45	−11.54
J1445+2702	−11.27	−11.54	−10.94	−10.45	−12.34	−11.92	−10.73	−10.99	−11.44	−12.04	−12.04
J1508-0011	−11.78	−12.47	−11.18	−10.69	−12.09	−11.75	−10.98	−11.29	−11.28	−11.86	−11.86
4FGL											
J0038-0207	−12.56	−12.70	−12.62	−12.14	−12.64	−13.47	−11.87	−11.95	−13.00	−13.46	−13.33
J0316+4119	−12.19	−12.5	−12.00	−11.52	−12.33	−13.05	−11.67	−12.17	−12.58	−12.77	−12.92
J0324+3410	−10.95	−10.96	−12.25	−11.76	−13.24	−12.71	−10.59	−10.61	−12.23	−12.52	−12.59
J0937+5008	−12.88	−12.95	−13.39	−12.91	−13.72	−14.54	−12.3	−12.39	−14.06	−13.31	−13.41
J0958+3224	−11.90	−11.94	−12.19	−11.71	−13.14	−12.47	−11.19	−11.20	−12.00	−12.18	−12.26
J1443+5201	−12.07	−12.19	−12.66	−12.18	−12.55	−13.45	−11.33	−11.39	−12.98	−13.04	−13.00
J1516+0015	−12.06	−12.35	−13.06	−12.58	−12.00	−12.32	−11.36	−11.42	−11.85	−12.54	−12.59
J2007-4434	−12.65	−12.70	−12.96	−12.48	−13.35	−13.81	−11.93	−11.94	−13.33	−13.12	−13.16
J2118+0013	−12.77	−12.81	−13.07	−12.59	−13.70	−14.00	−12.16	−12.21	−13.53	−13.67	−13.78
J2118-0732	−12.60	−12.91	−13.48	−13.00	−13.2	−13.45	−11.82	−12.02	−12.98	−13.94	−13.99
J2338+0326	−13.11	−13.41	−12.22	−11.74	−13.60	−12.51	−12.36	−12.43	−12.13	−12.66	−12.74

References

1. Seyfert, C.K. Nuclear emission in spiral nebulae. *Astrophys. J.* **1943**, *97*, 28–40. [CrossRef]
2. Weedman, D.W. High-velocity gas motions in galactic nuclei. *Astrophys. J.* **1970**, *159*, 405–413. [CrossRef]
3. Weedman, D.W. A Photometric study of Markarian galaxies. *Astrophys. J.* **1973**, *183*, 29–40. [CrossRef]
4. Khachikian, E.Y.; Weedman, D.W. A spectroscopic study of luminous galactic nuclei. *Astrophysics* **1971**, *7*, 231–240. [CrossRef]
5. Khachikian, E.Y.; Weedman, D.W. An atlas of Seyfert galaxies. *Astrophys. J.* **1974**, *192*, 581–589. [CrossRef]
6. Antonucci, R. Unified models for active galactic nuclei and quasars. *Annu. Rev. Astron. Astrophys.* **1993**, *31*, 473–521. [CrossRef]
7. Keel, W. Inclination effects on the recognition of Seyfert galaxies. *Astron. J.* **1980**, *85*, 198–203. [CrossRef]
8. Megan Urry, C.; Padovani, P. Unified schemes for radio-loud active galactic nuclei. *Publ. Astron. Soc. Pac.* **1995**, *107*, 803–845. [CrossRef]
9. Osterbrock, D.E.; Koski, A.T. NGC 4151 and Markarian 6—Two intermediate-type Seyfert galaxies. *Mon. Not. R. Astron. Soc.* **1976**, *176*, 61P–66P. [CrossRef]
10. Osterbrock, D.E. Spectrophotometry of Seyfert 1 galaxies. *Astrophys. J.* **1977**, *215*, 733–745. [CrossRef]
11. Whittle, M. Virial and jet-induced velocities in Seyfert galaxies. I. A compilation of narrow line region and host galaxy properties. *Astrophys. J. Suppl.* **1992**, *79*, 49–75. [CrossRef]
12. Netzer, H. AGN emission lines. In *Active Galactic Nuclei*; Courvoisier, T.J.-L., Mayor, M., Eds.; Springer: Berlin/Heidelberg, Germany, 1990; pp. 57–158. [CrossRef]
13. Järvelä, E.; Berton, M.; Ciroi, S.; Congiu, E.; Lähteenmäki, A.; Di Mille, F. SDSS J211852.96-073227.5: The first non-local, interacting, late-type intermediate Seyfert galaxy with relativistic jets. *Astron. Astrophys.* **2020**, *636*, L12. [CrossRef]
14. Foschini, L.; Lister, M.L.; Andernach, H.; Ciroi, S.; Marziani, P.; Antón, S.; Berton, M.; Dalla Bontà, E.; Järvelä, E.; Marchã, M.J.M.; et al. A New sample of gamma-ray emitting jetted active galactic nuclei. *Universe* **2022**, *8*, 587. [CrossRef]
15. Risaliti, G.; Elvis, M.; Bianchi, S.; Matt, G. Chandra monitoring of UGC 4203: The structure of the X-ray absorber. *Mon. Not. R. Astron. Soc. Lett.* **2010**, *406*, L20–L24. [CrossRef]
16. Storchi-Bergmann, T.; Nemmen da Silva, R.; Eracleous, M.; Halpern, J.P.; Wilson, A.S.; Filippenko, A.V.; Ruiz, M.T.; Smith, R.C.; Nagar, N.M. Evolution of the nuclear accretion disk emission in NGC 1097: Getting closer to the black hole. *Astrophys. J.* **2003**, *598*, 956–968. [CrossRef]
17. Peruzzi, T.; Pasquato, M.; Ciroi, S.; Berton, M.; Marziani, P.; Nardini, E. Interpreting automatic AGN classifiers with saliency maps. *Astron. Astrophys.* **2021**, *652*, A19. [CrossRef]
18. Foschini, L. The unification of relativistic jets. *Int. J. Mod. Phys.* **2014**, *28*, 1460188. [CrossRef]
19. Fossati, G.; Maraschi, L.; Ghisellini, G.; Celotti, A. A New Unifying Scheme for All Blazars. *Bull. Am. Astronom. Soc.* **1998**, *30*, 768. Available online: https://ui.adsabs.harvard.edu/abs/1998BAAS...30..768F/abstract (accessed on 22 October 2023).
20. Berton, M.; Björklund, I.; Lähteenmäki, A.; Congiu, E.; Järvelä, E.; Terreran, G.; La Mura, G. Line shapes in narrow-line Seyfert 1 galaxies: A tracer of physical properties? *Contrib. Astron. Obs. Skaln. Pleso* **2020**, *50*, 270–292. [CrossRef]
21. Riess, A.G.; Yuan, W.; Macri, L.M.; Scolnic, D.; Brout, D.; Casertano, S.; Jones, D.O.; Murakami, Y.; Anand, G.S.; Breuval, L.; et al. A comprehensive measurement of the local value of the Hubble constant with $1\,\mathrm{km\,s^{-1}\,Mpc^{-1}}$ uncertainty from the Hubble Space Telescope and the SH0ES team. *Astrophys. J. Lett.* **2022**, *934*, L7. [CrossRef]
22. The BAT AGN Spectroscopic Survey. Available online: http://www.bass-survey.com (accessed on 22 October 2023).
23. Peterson, B.M. *An Introduction to Active Galactic Nuclei*; Cambridge University Press: Cambridge, UK, 2003. [CrossRef]
24. Abdollahi, S.; Acero, F.; Ackermann, M.; Ajello, M.; Atwood, W.B.; Axelsson, M.; Baldini, L.; Ballet, J.; Barbiellini, G.; Bastieri, D.; et al. *Fermi* Large Area Telescope fourth source catalog. *Astrophys. J. Suppl. Ser.* **2020**, *247*, 33. [CrossRef]
25. Baldwin, J.A.; Phillips, M.M.; Terlevich, R. Classification parameters for the emission-line spectra of extragalactic objects. *Publ. Astron. Soc. Pac.* **1981**, *93*, 5–19. [CrossRef]
26. Veilleux, S.; Osterbrock, D.E. Spectral classification of emission-line galaxies. *Astrophys. J. Suppl.* **1987**, *63*, 295–310. [CrossRef]
27. Heckman, T.M. An optical and radio survey of the nuclei of bright galaxies. Activity in the normal galactic nuclei. *Astron. Astrophys.* **1980**, *87*, 152–164. Available online: https://ui.adsabs.harvard.edu/abs/1980A%26A....87..152H/ (accessed on 22 October 2023).
28. PyAstronomy: dopplerShift.py. Available online: https://github.com/sczesla/PyAstronomy/blob/master/src/pyasl/asl/dopplerShift.py (accessed on 22 October 2023).
29. Cardelli, J.A.; Clayton, G.C.; Mathis, J.S. The relationship between infrared, optical, and ultraviolet extinction. *Astrophys. J.* **1989**, *345*, 245–256. [CrossRef]
30. Bohlin, R.C.; Savage, B.D.; Drake, J.F. A survey of interstellar H I from Lalpha absorption measurements. II. *Astrophys. J.* **1978**, *224*, 132–142. [CrossRef]
31. NASA's HEASARC: Tools. N_H. Available online: https://heasarc.gsfc.nasa.gov/cgi-bin/Tools/w3nh/w3nh.pl (accessed on 22 October 2023).
32. Letawe, G.; Magain, P.; Courbin, F.; Jablonka, P.; Jahnke, K.; Meylan, G.; Wisotzki, L. On-axis spectroscopy of the host galaxies of 20 optically luminous quasars at $z \sim 0.3$. *Mon. Not. R. Astron. Soc.* **2007**, *378*, 83–108. [CrossRef]
33. Mannucci, F.; Basile, F.; Poggianti, B.M.; Cimatti, A.; Daddi, E.; Pozzetti, L.; Vanzi, L. Near-infrared template spectra of normal galaxies: *k*-corrections, galaxy models and stellar populations. *Mon. Not. R. Astron. Soc.* **2001**, *326*, 745–758. [CrossRef]

34. Kovačević, J.; Popović, L.Č.; Dimitrijević, M.S. Analysis of optical Fe II emission in a sample of AGN spectra. *Astrophys. J. Suppl.* **2010**, *189*, 15–36. [CrossRef]

35. Shapovalova, A.I.; Popović, L.Č.; Burenkov, A.N.; Chavushyan, V.H.; Ilić, D.; Kovačević, A.; Kollatschny, W.; Kovačević, J.; Bochkarev, N.G.; Valdes, J.R.; et al. Spectral optical monitoring of the narrow-line Seyfert 1 galaxy Ark 564. *Astrophys. J. Suppl. Ser.* **2012**, *202*, 10. [CrossRef]

36. Fe II Template. Available online: http://servo.aob.rs/FeII_AGN/link6.html (accessed on 22 October 2023).

37. Dimitrijević, M.S.; Kovačević, J.; Popović, L.Č.;, Dačić, M.; Ilić, D.; The flux ratio of the [O III]$\lambda\lambda$4959, 5007 Å lines in AGN. *AIP Conf. Proc.* **2007**, *895*, 313–316. [CrossRef]

38. Tachiev, G.; Fischer, C. Breit-Pauli energy levels and transition rates for the carbonlike sequence. *Can. J. Phys.* **2001**, *79*, 955–976. [CrossRef]

39. NIST: Physical Measurement Laboratory. Atomic Spectra Database. Available online: https://www.nist.gov/pml/atomic-spectra-database (accessed on 22 October 2023).

40. astrophy:docs. Models and Fitting. Available online: https://docs.astropy.org/en/stable/modeling/ (accessed on 22 October 2023).

41. Boroson, T. Blueshifted [O III] emission: Indications of a dynamic narrow-line region. *Astron. J.* **2005**, *130*, 381–386. [CrossRef]

42. Smith, K.L.; Mushotzky, R.F.; Vogel, S.; Shimizu, T.T.; Miller, N. Radio properties of the BAT AGNs: The FIR-radio relation, the fundamental plane, and the main sequence of star formation. *Astrophys. J.* **2016**, *832*, 163. [CrossRef]

43. Yang, J.; van Bemmel, I.; Paragi, Z.; Komossa, S.; Yuan, F.; Yang, X.; An, T.; Koay, J.Y.; Reynolds, C.; Oonk, J.B.R.; et al. A parsec–scale faint jet in the nearby changing-look Seyfert galaxy Mrk 590. *Mon. Not. R. Astron. Soc. Lett.* **2021**, *502*, L61–L65. [CrossRef]

44. Doi, A.; Inoue, Y. High–frequency excess in the radio continuum spectrum of the type-1 Seyfert galaxy NGC 985. *Publ. Astron. Soc. Jpn.* **2016**, *68*, 56. [CrossRef]

45. Järvelä, E.; Dahale, R.; Crepaldi, L.; Berton, M.; Congiu, E.; Antonucci, R. Unravelling the origin of extended radio emission in narrow–line Seyfert 1 galaxies with the JVLA. *Astron. Astrophys.* **2022**, *658*, A12. [CrossRef]

46. Kauffmann, G.; Heckman, T.M.; Tremonti, C.; Brinchmann, J.; Charlot, S.; White, S.D.M.; Ridgway, S.E.; Brinkmann, J.; Fukugita, M.; Hall, P.B.; et al. The host galaxies of active galactic nuclei. *Mon. Not. R. Astron. Soc.* **2003**, *346*, 1055–1077. [CrossRef]

47. Kewley, L.J.; Groves, B.; Kauffmann, G.; Heckman, T. The host galaxies and classification of active galactic nuclei. *Mon. Not. R. Astron. Soc.* **2006**, *372*, 961–976. [CrossRef]

48. Buttiglione, S.; Capetti, A.; Celotti, A.; Axon, D.J.; Chiaberge, M.; Macchetto, F.D.; Sparks, W.B. An optical spectroscopic survey of the 3CR sample of radio galaxies with $z < 0.3$. II. Spectroscopic classes and accretion modes in radio-loud AGN. *Astron. Astrophys.* **2010**, *509*, A6. [CrossRef]

49. Heckmann, T.M.; Ptak, A.; Hornschemeier, A.; Kauffmann, G. The relationship of hard X-Ray and optical line emission in low–redshift active galactic nuclei. *Astrophys. J.* **2005**, *634*, 161–168. [CrossRef]

50. Risaliti, G.; Salvati, M.; Marconi, A. [O III] equivalent width and orientation effects in quasars. *Mon. Not. R. Astron. Soc.* **2011**, *411*, 2223–2229. [CrossRef]

51. Marin, F. Are there reliable methods to estimate the nuclear orientation of Seyfert galaxies? *Mon. Not. R. Astron. Soc.* **2016**, *460*, 3679–3705. [CrossRef]

52. Haas, M.; Siebenmorgen, R.; Schulz, B.; Krügel, E.; Chini, R. Spitzer IRS spectroscopy of 3CR radio galaxies and quasars: Testing the unified schemes. *Astron. Astrophys.* **2005**, *442*, L39–L43. [CrossRef]

53. Baum, S.A.; Gallimore, J.F.; O'Dea, C.P.; Buchanan, C.L.; Noel-Storr, J.; Axon, D.J.; Robinson, A.; Elitzur, M.; Dorn, M.; Staudaher, S. Infrared diagnostics for the extended 12 μm Sample of Seyferts. *Astrophys. J.* **2010**, *710*, 289–308. [CrossRef]

54. Dalla Barba, B.; Foschini, L. X-ray properties of two complementary samples of Intermediate Seyfert galaxies. 2023, *in preparation*.

55. Osterbrock, D.E.; Ferland, G.J. *Astrophysics of Gaseous Nebulae and Active Galactic Nuclei*; University Science Books: Sausalito, CA, USA, 2006. Available online: https://archive.org/details/astrophysicsofga0000oste (accessed on 22 October 2023).

56. Binette, L.; Raga, A.C.; Calvet, N.; Canto, J. Balmer decrements in Seyfert 2 galaxies. *Publ. Astron. Soc. Pac.* **1990**, *102*, 723–725. [CrossRef]

57. Nagao, T.; Murayama, T.; Taniguchi, Y. Seyfert-type dependences of narrow emission-line ratios and physical properties of high-ionization nuclear emission-line regions in Seyfert galaxies. *Publ. Astron. Soc. Jpn.* **2001**, *53*, 629–645. [CrossRef]

58. Schnorr-Müller, A.; Davies, R.I.; Korista, K.T.; Burtscher, L.; Rosario, D.; Storchi-Bergmann, T.; Contursi, A.; Genzel, R.; Graciá-Carpio, J.; Hicks, E.K.S.; et al. Constraints on the broad-line region properties and extinction in local Seyferts. *Mon. Not. R. Astron. Soc.* **2016**, *462*, 3570–3590. [CrossRef]

59. Dong, X.; Wang, T.; Wang, J.; Yuan, W.; Zhou, H.; Dai, H.; Zhang, K. Broad-line Balmer decrements in blue active galactic nuclei. *Mon. Not. R. Astron. Soc.* **2008**, *383*, 581–592. [CrossRef]

60. La Mura, G.; Popović, L.Č, Ciroi, S.; Rafanelli, P.; Ilić, D. Detailed analysis of Balmer lines in a Sloan Digital Sky Survey sample of 90 broad-line active galactic nuclei. *Astrophys. J.* **2007**, *671*, 104–117. [CrossRef]

61. Schmitt, H.R.; Kinney, A.L. A Comparison between the narrow-line regions of Seyfert 1 and Seyfert 2 galaxies. *Astrophys. J.* **1996**, *463*, 498–508. [CrossRef]

62. Kinney, A.L.; Schmitt, H.R.; Clarke, C.J.; Pringle, J.E.; Ulvestad, J.S.; Antonucci, R.R.J. Jet directions in Seyfert galaxies. *Astrophys. J.* **2000**, *537*, 152–177. [CrossRef]

63. Nagar, N.M.; Wilson, A.S. The relative orientation of nuclear accretion and galaxy stellar disks in Seyfert galaxies. *Astrophys. J.* **1999**, *516*, 97–113. [CrossRef]

64. Gaskell, C.M.; Harrington, P.Z. Partial dust obscuration in active galactic nuclei as a cause of broad-line profile and lag variability, and apparent accretion disc inhomogeneities. *Mon. Not. R. Astron. Soc.* **2018**, *478*, 1660–1669. [CrossRef]

65. Koss, M.; Trakhtenbrot, B.; Ricci, C.; Lamperti, I.; Oh, K.; Berney, S.; Schawinski, K.; Balokovic, M.; Baronchelli, L.; Crenshaw, D.M.; et al. BAT AGN spectroscopic survey. I. Spectral measurements, derived quantities, and AGN demographics. *Astrophys. J.* **2017**, *850*, 74. [CrossRef]